JOURNAL OF MATERIALS SCIENCE 27 (1992) 5895–5904

Analytical electron microscopy of Al_2O_3 implanted with iron ions

P. S. SKLAD, C. J. McHARGUE, C. W. WHITE
Oak Ridge National Laboratory, Oak Ridge, TN 37831, USA
G. C. FARLOW
Wright State University, Dayton, OH 45435, USA

Single crystals of α-Al_2O_3 were implanted with iron ions at room temperature to fluences ranging from 4×10^{16} Fe cm^{-2} to 1×10^{17} Fe cm^{-2}. The microstructure and composition in the implanted region were examined using analytical electron microscopy techniques. Special emphasis was placed on monitoring the microstructural changes which take place during post-implantation annealing. Clusters of metallic α-Fe were identified in the specimen after implantation to a dose of 1×10^{17} Fe cm^{-2}. Analytical electron microscopy of implanted specimens annealed in oxygen revealed the redistribution of the implanted iron and the formation of surface precipitates of α-Fe_2O_3, subsurface precipitates of various forms of spinel, and, in some cases, subsurface precipitates of iron, depending on the annealing temperature. Examination of implanted specimens annealed under reducing conditions revealed the presence of precipitates of α-Fe.

1. Introduction

Over the last several years a great deal of effort has been expended on improving the surface-related properties of materials through the alteration of the near-surface region by ion implantation [1]. Most of the effort has been expended on developing metals and semiconductors. In fact, ion-beam modification of these two classes of materials has reached a point of successful commercialization. More recently, ion-implantation techniques have been applied to the modification of surface properties of ceramic materials [2–4]. Because of its importance as a technological material, Al_2O_3 has received most of the attention.

During the ion-implantation process, energetic ions impinge on the surface of the material and displace atoms from their normal lattice sites by atomic collisions. In the case of Al_2O_3, the aluminium and oxygen are distributed over two distinct sublattices so that atoms of one type which are displaced are not likely to come to rest on the lattice sites of the other species. In addition, the displacement energies of aluminium and oxygen are substantially different [5]. Depending on the implantation conditions, the vacancies and interstitials so produced may recombine or partition into extended defects. Owing to the nature of the ionic bonding in Al_2O_3, the defects which are produced must be in the form of charged point defects or stoichiometric in nature. Upon losing sufficient energy, ions implanted at moderate energies (a few hundred keV) come to rest typically within a few tenths of a micrometre from the surface. Because most of the ions come to rest in the region where the defect production is high, a number of considerations must be included in analysing the resultant microstructural changes: alloying effects, defect configurations, implanted species–defect interactions, nonequilibrium lattice positions of the injected ions, and charge imbalance. Whereas the investigation of these defects and their interactions is important, the effectiveness of the surface treatment is also strongly dependent on the microstructural development which takes place during post-implantation annealing. This is particularly important in the case of Al_2O_3 because many of the potential applications involve high temperatures.

In order to exploit successfully the beneficial effects of surface modification, it is necessary to understand the microstructural evolution leading to the property changes. Transmission electron microscopy (TEM) and, in particular, analytical electron microscopy (AEM), has been shown to be a valuable technique for the study of ion-implantated materials [6, 7]. The techniques of AEM that are the most useful are X-ray energy dispersive spectroscopy (EDS), electron energy loss spectroscopy (EELS), and convergent beam electron diffraction (CBED), in addition to conventional imaging and diffraction methods. These techniques are unique in that they allow direct observation and characterization of solute concentration profiles, second-phase formation, lattice damage, crystallinity of the implanted layer, and the annealing behaviour of the material. Such analyses allow correlations to be made with theoretical models, property measurements, and the results of complementary techniques such as Rutherford backscattering spectroscopy (RBS) and conversion-electron Mössbauer spectroscopy (CEMS).

The physical and structural changes which take place in Al_2O_3 implanted with iron ions have been investigated previously with the use of RBS and CEMS [8] and also in preliminary TEM investigations [6, 9–12]. This paper presents the results of an AEM investigation of similar materials. Special emphasis is placed on the microstructural development which takes place during post-implantation annealing as a function of both annealing temperature and environment.

2. Experimental procedure

The material used in this study was high-purity α-Al_2O_3 in the basal orientation (surface normal [0001]). All specimens were given an optical grade surface polish followed by a 5 day anneal at 1400 °C in flowing oxygen to remove any residual surface damage. Single-crystal specimens were then implanted at room temperature with 160 keV iron ions to a dose of 4×10^{16} or 1×10^{17} Fe cm^{-2} at a dose rate of $\sim 2\ \mu A\ cm^{-2}$. Beam heating was estimated to be less than 150 °C [4]. The crystals were implanted with the ion beam $\sim 7°$ off-normal to minimize channelling effects. A number of specimens were subsequently annealed for 1 h in the range 700–1500 °C in flowing oxygen or in a flowing mixture of 96% argon and 4% hydrogen.

Because the regions of interest are located within several hundred nanometres of the surface, it has proved useful to examine both cross-sectional and backthinned specimens in order to obtain a complete understanding of the microstructures that develop and their relationship to the surface. Details of the preparation procedure are reported elsewhere [13, 14]. In general, information regarding depth dependence is obtained from the examination of cross-sectioned specimens, whereas measurements which require larger areas for analysis are obtained from backthinned specimens. Microscopy was performed with the use of a Philips EM400T/FEG operated at 100 kV and a Philips EM430T operated at 300 kV. Both instruments were equipped with 6585 STEM and EDAX 9100/70 X-ray EDS systems. Selected specimens were also examined in a VG HB501 UX scanning transmission electron microscope (STEM). Double-tilt specimen holders with beryllium cups were used for all EDS measurements in order to minimize the X-ray systems background [15]. For the same reason, support rings used to provide mechanical stability for cross-sectioned specimens were manufactured from graphite. Liquid-nitrogen-cooled, double-tilt, beryllium specimen holders were used to minimize contamination for those EDS measurements requiring high current density, small-diameter electron probes.

3. Results and discussion

3.1. As-implanted material

The microstructure observed in the as-implanted material is typical of many implanted ceramics, i.e. a tangled array of dislocations extending from the surface over the entire depth of implantation, ~ 170 nm, as shown in Fig. 1 for a cross-sectioned specimen implanted to a dose of 4×10^{16} Fe cm^{-2}. The corresponding electron microdiffraction pattern confirms the crystalline nature of the implanted layer. No evidence of a precipitated second phase can be seen in either the micrograph or the diffraction pattern. Although the fine scale of the damage, together with the thickness of the specimen, make it difficult to characterize the exact nature of the defects, the dislocation arrays are similar to those observed in Al_2O_3 following neutron irradiation [16, 17], ion implantation [18–21] and electron irradiations [22–25]. In these studies of irradiated Al_2O_3 it has been shown that the dislocation tangles develop from faulted, interstitial loops that nucleate on (0001). These loops subsequently unfault, grow, and eventually intersect to form networks. A smaller number of $\{10\bar{1}0\}$ loops are also formed.

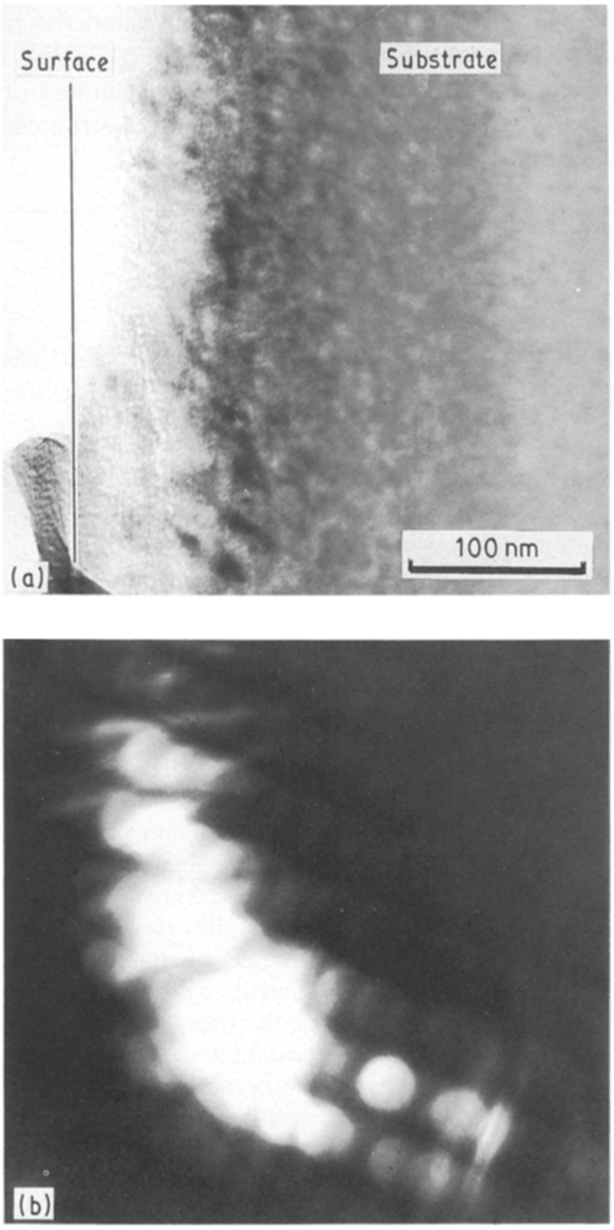

Figure 1 (a) Microstructure of α-Al_2O_3 implanted at room temperature with 160 keV ^{56}Fe ions to a dose of 4×10^{16} Fe cm^{-2}, cross-sectioned specimen; (b) convergent beam electron diffraction pattern from implanted layer.

Measurements of the iron content of this implanted region were made by X-ray EDS while operating in the scanning transmission electron microscopy (STEM) mode. This technique is sensitive only to elements with atomic number, Z, > 11. Nonetheless, the results obtained give a reasonable picture of the cation distribution in the specimen volume examined. The FeK_α peak, AlK_α peak, and respective background regions were recorded over 30 intervals as the electron probe moved continuously from a depth of 250 nm toward the surface. The spreading of the electron beam as it passes through the specimen and the uncertainty in position of the moving beam as it scans the specimen combine to limit the spatial resolution to 10–12 nm. After appropriate background and hole count subtraction, quantification was carried out employing integrated peak intensities and the standardless analysis routines developed by Zaluzec [26]. The results are plotted in Fig. 2 as the ratio of iron to aluminium versus depth. The iron concentration profile shows a well-defined peak at ~ 60 nm from the surface and a maximum Fe/Al atom fraction of $\sim 9.5\%$. The Fe/Al ratio drops to a minimal value at a depth of ~ 180 nm. The area under the curve is directly proportional to the total iron content of the specimen.

Examination of a specimen implanted to 1×10^{17} Fe cm^{-2} (a dose 2.5 times greater than the dose considered above) revealed a dislocation microstructure similar to that seen in the lower dose case. In addition, the higher dose material exhibited a region of less dense material, as shown by the light band located below the implanted surface in Fig. 3. This region corresponds approximately to the region of maximum ion damage and may indicate the initial stages of amorphization. This observation is confirmed by the RBS spectra shown in Fig. 4. The aligned spectrum for the aluminium is nearly coincident with the random spectrum over a small distance below the implanted surface which is an indication of amorphous material. These observations are consistent with suggestions that damage accumulation would lead to amorphization in α-Al$_2$O$_3$ implanted with 160 keV iron to fluences only slightly greater than 1×10^{17} Fe cm^{-2} [2]. It should also be noted that the implanted layer in this specimen extends slightly deeper into the material, 220–230 nm, than observed in other specimens implanted at the same energy. The reason for the discrepancy is not known. Examination of a backthinned specimen of the material implanted to 1×10^{17} Fe cm^{-2} revealed the presence of 1–3 nm diameter darkly imaging features, Fig. 5. Approximately 50 nm had been intentionally removed from the implanted surface of this specimen by ion milling so that the newly exposed surface corresponds nearly to the location of the peak in the iron concentration profile as measured by EDS line scans. X-ray EDS measurements using a 2–3 nm diameter electron probe showed that these features are iron rich. The diffuse satellite spots in the selected-area diffraction (SAD) pattern, shown in the inset in Fig. 5, are consistent with the clusters being body centred cubic α-Fe oriented such that the $\langle 1\,1\,1 \rangle$ α-Fe//[0 0 0 1] α-Al$_2$O$_3$.

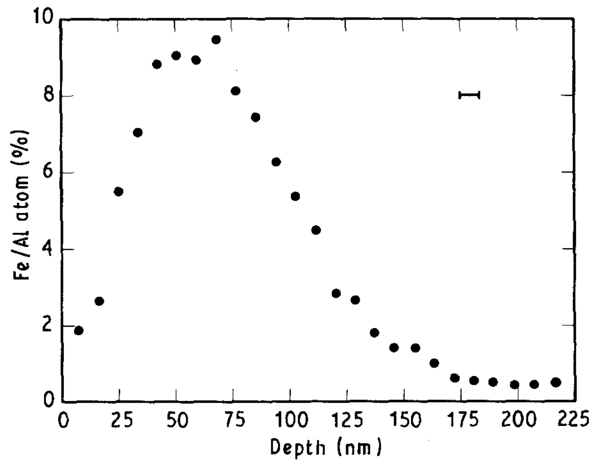

Figure 2 Iron concentration profile obtained from X-ray EDS line scan across the implanted layer of the specimen shown in Fig. 1.

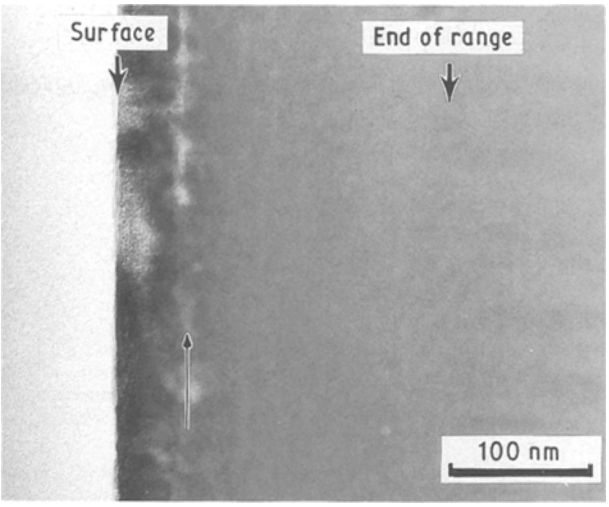

Figure 3 Microstructure of α-Al$_2$O$_3$ implanted at room temperature with 160 keV ^{56}Fe to a dose of 1×10^{17} Fe cm^{-2}, cross-sectioned specimen. Arrow indicates region of less-dense material.

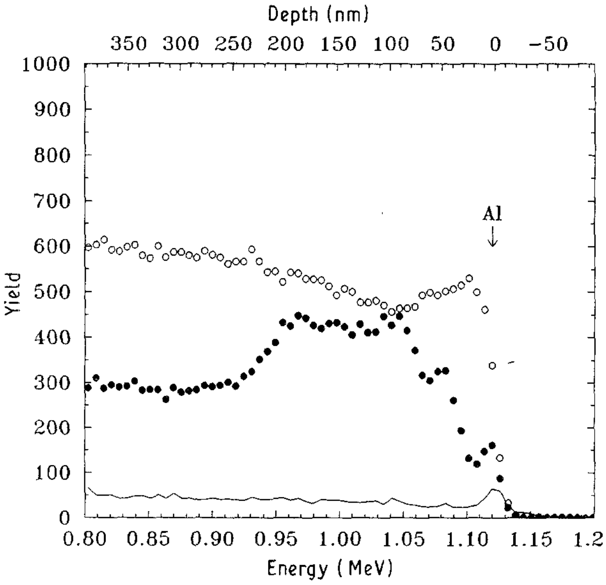

Figure 4 RBS spectra for specimen shown in Fig. 3: (○) random, (●) aligned, (——) virgin, aligned.

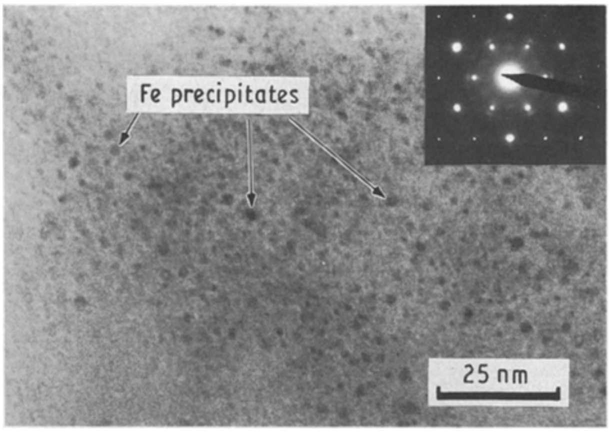

Figure 5 Microstructure of α-Al_2O_3 implanted at room temperature with 160 keV ^{56}Fe to a dose of 1×10^{17} Fe cm^{-2}, backthinned specimen. Inset is the selected-area diffraction pattern.

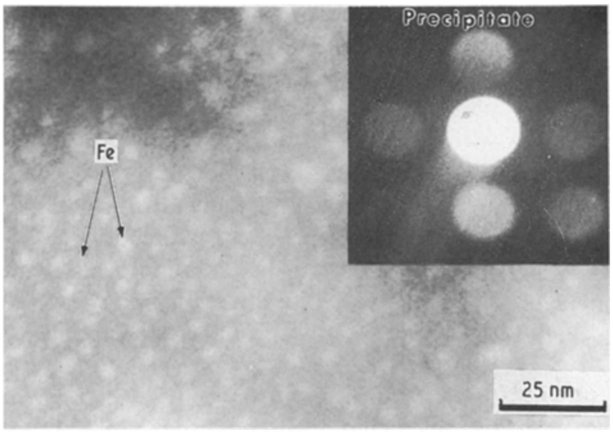

Figure 6 *Z*-contrast STEM image of as-implanted microstructure in α-Al_2O_3 implanted with 1×10^{17} Fe cm^{-2} at room temperature. Inset is a convergent beam electron diffraction pattern from a single iron cluster.

In order to confirm the identification of the clusters, the specimen was examined by STEM *Z*-contrast imaging. This technique utilizes electrons scattered through large angles ($\sim 5°$), where the electron scattering is strongly sensitive to atomic number, *Z* [27]. By placing a high-angle annular detector around the transmitted beam it is possible to obtain images which show strong *Z*-contrast but with minimal diffraction (strain) contrast due to structural features. A *Z*-contrast image is complementary to a conventional diffraction contrast image (e.g. Fig. 5) which is primarily sensitive to structure, but relatively insensitive to atomic composition. In addition, with the HB501 UX equipped with a special pole piece, it is possible to obtain images at high spatial resolution (0.25 nm). Fig. 6 shows such a *Z*-contrast image. The fine electron probe also makes it possible to obtain CBED patterns from individual clusters. The CBED pattern shown in the inset is consistent with diffraction from body-centred cubic α-Fe.

The results presented above suggest that the implanted iron ions are present in the expected distribution within the near-surface implanted region. It is assumed that due to the relatively low implantation temperature the iron ions come to rest in non-equilibrium lattice sites. The high damage level is responsible for the presence of high concentrations of point defects, such as vacancies and interstitials, as well as the high dislocation density seen in the microstructure. Whereas it is unlikely that any long-range diffusion processes are operative at the temperatures experienced during implantation ($< 200\,°C$), the observation of α-Fe in the specimen implanted to 1×10^{17} Fe cm^{-2} suggests that the implanted iron undergoes short-range clustering processes.

3.2. Annealing in oxygen

Various AEM techniques have also been applied to the characterization of the microstructural development which takes place during annealing in oxygen. In order to investigate the possible redistribution of iron during annealing, X-ray EDS line scans were used to obtain iron composition profiles from specimens implanted to 1×10^{17} Fe cm^{-2} and annealed for 1 h at 700 or 900 °C. Reliable EDS line scans could not be obtained from a specimen implanted to 1×10^{17} Fe cm^{-2}. Therefore, the EDS measurements from the annealed specimens are compared to the results for the as-implanted (4×10^{16} Fe cm^{-2}) specimen (Fig. 7). All three specimens exhibit a peak in the Fe/Al profile below the implanted surface. As described above, the maximum Fe/Al atom fraction for the as-implanted specimen is $\sim 9.5\%$. In comparison, the maximum Fe/Al for the specimen annealed at 700 °C is $\sim 26\%$, a factor of 2.5 times higher, as might be expected from the dose. In contrast, the specimen annealed at 900 °C, although implanted to the higher dose, exhibits a maximum Fe/Al atom fraction of only 13.5%. This reduced value for the iron concentration indicates that approximately one-half of the implanted iron has diffused away from the as-implanted peak depth during the anneal at 900 °C. It is also important to note that the peak in the iron to aluminium ratio for this specimen occurs at ≈ 45 nm from the surface and that the value of the ratio just below the specimen surface is $\sim 4\%$, noticeably higher than measured in either of the other two specimens. These latter observations are consistent with significant redistribution of iron toward the surface during the 900 °C anneal. The EDS results from the specimen annealed at 900 °C also indicated a significant enrichment of iron in a region on the original specimen surface. Although the actual values obtained are difficult to present quantitatively in Fig. 7 because they are so large, it is reasonable to deduce that these regions are almost 100% iron.

The microstructure observed in a cross-sectioned specimen implanted with 1×10^{17} Fe cm^{-2} and annealed in oxygen for 1 h at 700 °C is shown in Fig. 8. A band of precipitates, 2–4 nm diameter, can be seen lying in a region corresponding to the maximum in the as-implanted iron distribution, extending from 50–90 nm from the surface. A few of the precipitates are as large as 6 nm. The identity of these precipitates was not determined from TEM. However, CEMS

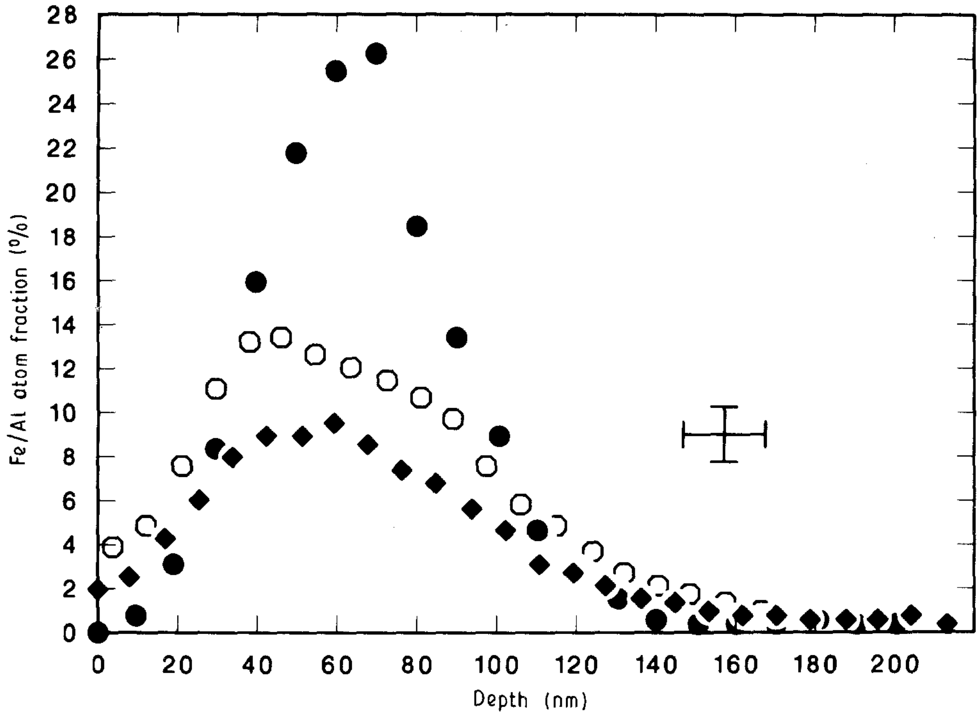

Figure 7 Comparison of iron concentration profiles determined by X-ray energy dispersive spectroscopy for specimens implanted with iron at room temperature and annealed for 1 h in oxygen. (◆) 4×10^{16} Fe cm^{-2}, as-implanted; (●) 1×10^{17} Fe cm^{-2}, at 700 °C; (○) 1×10^{17} Fe cm^{-2}, at 900 °C.

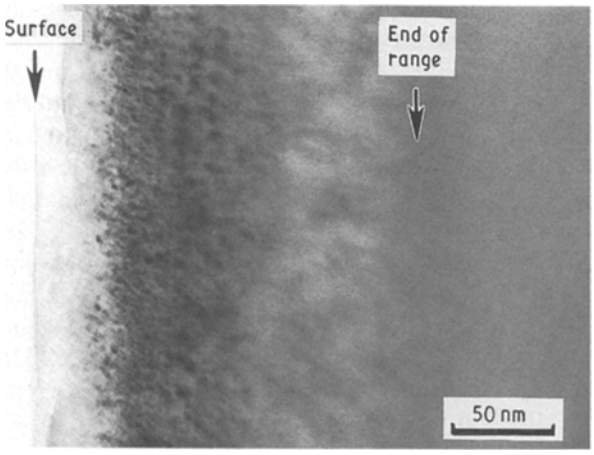

Figure 8 Microstructure of α-Al_2O_3 implanted with 1×10^{17} Fe cm^{-2} and annealed for 1 h at 700 °C in oxygen, cross-sectioned specimen.

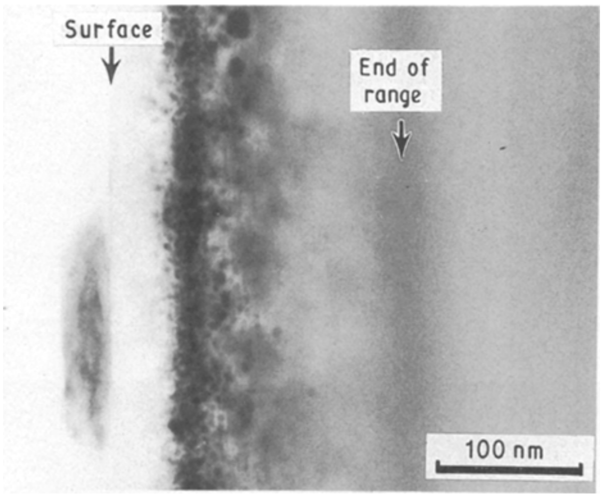

Figure 9 Microstructure of α-Al_2O_3 implanted with 4×10^{16} Fe cm^{-2} and annealed for 1 h at 900 °C in oxygen, cross-sectioned specimen.

suggests that they may be mixed oxides of the type $FeAl_2O_4$ [8].

The microstructural development responsible for the changes produced in the iron concentration profile by annealing at 900 °C was investigated by the examination of specimens implanted to doses of 4×10^{16} Fe cm^{-2} or 1×10^{17} Fe cm^{-2} and annealed in oxygen at 900 °C. The microstructure observed in a cross-sectioned specimen is composed of several regions as shown in Fig. 9. The first region consists of ledge-like features on the original specimen surface. The ledges are relatively uniform in width, 35–40 nm, and range in lateral dimension from 180–310 nm. A second region is relatively featureless except for a small number of faceted cavities. Centred at a depth of ≈ 57 nm is a band of precipitates, ~ 5 nm diameter. A few larger precipitates, 10–12 nm diameter, as well as some faceted cavities, are present slightly below the band. X-ray microanalysis indicated that all of the precipitates examined were rich in iron. The region extending from ~ 125 to ~ 200 nm also appears featureless. However, this may be due in part to the specimen thickness which may obscure some of the microstructural detail, such as dislocations. Finally, at a depth of ~ 200 nm, a dark band which corresponds to the end-of-range damage characteristic of ion implanted specimens is observed. For a more complete discussion of this type of defect structure see the review by Bentley [7].

In order to obtain complementary information as to the nature of the precipitates observed in Fig. 9, for the specimen annealed at 900 °C, a specimen prepared by backthinning was examined. This examination revealed a microstructure characterized by large faceted precipitates, a distribution of smaller precipitates, a loose network of dislocations, and a distribution of cavities. The large precipitates and the small 5 nm precipitates are shown in Moiré fringe contrast in Fig. 10a and b, respectively. The size of the large precipitates is approximately 200 nm which compares well with the size of the ledges shown in Fig. 9. Fig. 10c is a selected-area diffraction pattern that includes reflections from the matrix as well as both types of precipitates. The most intense reflections in the pattern correspond to the [0 0 0 1] zone axis pattern of the Al_2O_3 matrix. Subsidiary spots are also observed. Taking double diffraction effects into account, it is possible to ascribe the spots labelled H to the [0 0 0 1] zone axis of Fe_2O_3, haematite. The complex pattern of the Moiré fringe spacings on the large precipitates in Fig. 10a indicates that the precipitates may contain defects such as faults or twins. In addition, the bend contours visible in the image indicate that the specimen is buckled. Nevertheless, measurement of the fringe spacings in areas which appear relatively undisturbed yielded values of 4.5 and 2.5 nm. These values agree well with calculated values of 4.6 nm determined using the $\{1 1 \bar{2} 0\}$ Al_2O_3 and the $\{1 1 \bar{2} 0\}$ Fe_2O_3 diffracted beams, and 2.6 nm using the $\{0 3 \bar{3} 0\}$ Al_2O_3 and the $\{0 3 \bar{3} 0\}$ Fe_2O_3 beams. Analysis of the Moiré fringe spacing and the diffraction pattern indicates that the precipitates are oriented such that [0 0 0 1] α-Fe_2O_3//[0 0 0 1] α-Al_2O_3. The subsidiary spots labelled S in the diffraction pattern, correspond to diffraction from the smaller precipitates. Analysis of the Moiré fringe spacings in Fig. 10b suggest the presence of two types of precipitate, both with 1.4 nm spacings. One set of precipitates exhibits three sets of fringes 60° apart. Analysis of these fringes and the corresponding diffraction evidence indicate interference between $\{1 1 \bar{2} 0\}$ Al_2O_3 and $\{1 1 0\}$ α-Fe and are consistent with an orientation relationship such that $\langle 1 1 1 \rangle$ α-Fe//[0 0 0 1] α-Al_2O_3. This orientation relationship was also reported by Ohkubo *et al.* [28]. Other precipitates are observed which exhibit a single set of fringes with 1.4 nm spacings. These precipitates may be identified as $FeAl_2O_4$ spinel precipitates which are oriented such that $\langle 1 1 0 \rangle$ spinel//[0 0 0 1] α-Al_2O_3. The fringes would be produced by interference between the $\{1 1 \bar{2} 0\}$$Al_2O_3$ and the $\{4 0 0\}$ $FeAl_2O_4$ diffracted beams. The most common orientation relationship reported by other investigators for spinel-sesquioxide systems is $\langle 1 1 1 \rangle$ spinel // [0 0 0 1] Al_2O_3 (e.g. for $CoAl_2O_4$ and Al_2O_3 [29], $NiAl_2O_4$ and Al_2O_3 [30, 31], $MnAl_2O_4$ and Al_2O_3 [31], and Fe_2O_3 and $NiAl_2O_4$ [32]), although some variations have been seen (e.g. for $NiAl_2O_4$ in Al_2O_3 [30], $FeAl_2O_4$ in Al_2O_3 [32], and (Al, $Fe)_3O_4$ in (Al, $Fe)_2O_3$ [33]). It should be noted that a single set of Moiré fringes with 1.4 nm spacing may also be produced by interference between the $\{1 1 \bar{2} 0\}$ Al_2O_3 and the $\{4 0 0\}$ Fe diffracted beams, consistent with an orientation relationship such that $\langle 1 1 0 \rangle$ Fe// [0 0 0 1] α-Al_2O_3. This latter orientation relationship will be discussed later with respect to specimens annealed in 96%Ar/4%H_2. The observation of both metallic α-Fe and $FeAl_2O_4$ precipitates in this specimen may be related to the diffusion of oxygen into the subsurface region. In the case of high annealing temperatures or long annealing times, oxygen may diffuse sufficiently deep to oxidize all the iron. However, if the temperature is too low or the annealing time is too short, the oxygen will not

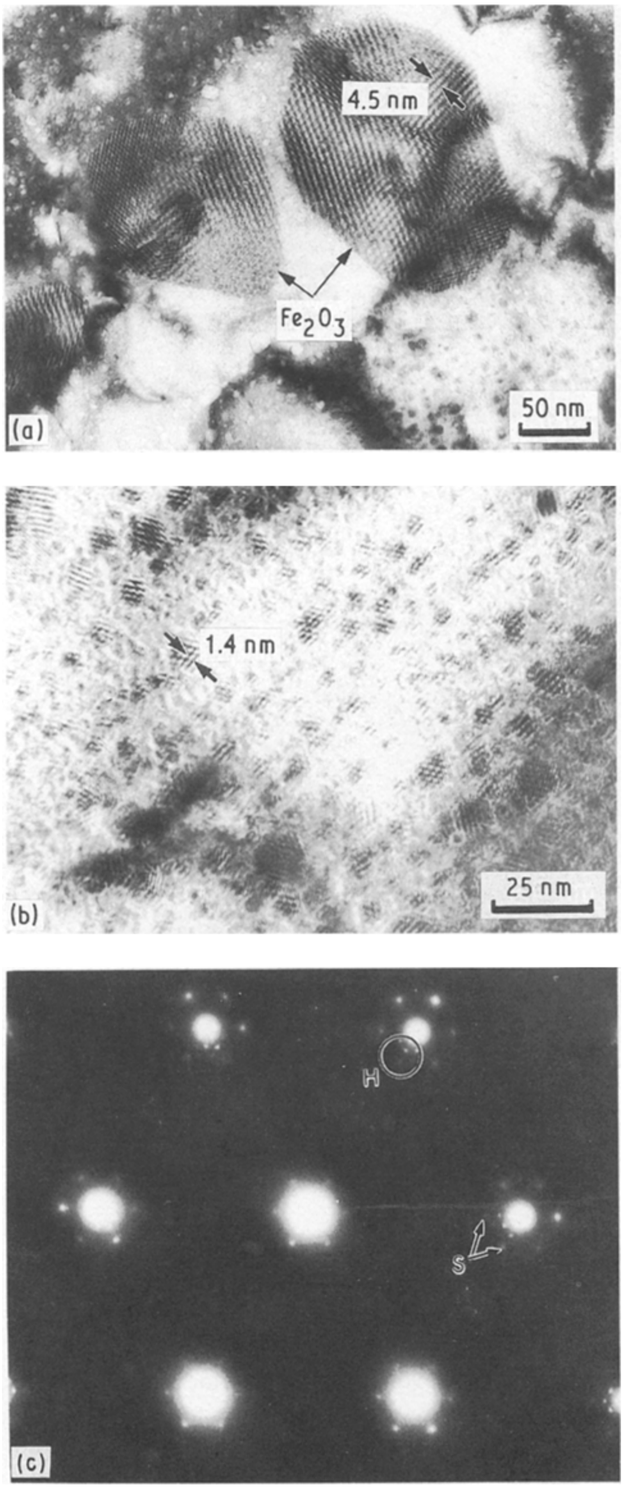

Figure 10 Microstructure of α-Al_2O_3 implanted with 1×10^{17} Fe cm^{-2} and annealed for 1 h at 900 °C in oxygen, backthinned specimen: (a) Moiré image of Fe_2O_3 surface precipitates, (b) Moiré image of subsurface precipitates, (c) selected-area diffraction pattern from specimen shown in (a) and (b). Intense reflections correspond to the $\langle 0 0 0 1 \rangle$ zone axis pattern of α-Al_2O_3; reflections labelled H correspond to $\langle 0 0 0 1 \rangle$ zone axis pattern of Fe_2O_3; reflections labelled S correspond to diffraction from subsurface precipitates.

be able to diffuse deep enough to reach all of the implanted iron. Such observations have been made in other investigations [31].

The results of CEMS measurements [8] on similar specimens suggest the presence of two types of precipitate, α-Fe_2O_3 and a spinel-like phase ($FeAl_2O_4$ or Fe_3O_4) containing Fe^{3+}. The spinel phase must have a defect structure similar to γ-Al_2O_3 [8] because in this structure the unit cell contains only 3 + cations and has cation vacancies randomly distributed on the octahedral sites. The CEMS results also suggest that it is likely that the precipitates contain small amounts of Al^{3+}. The results presented by McHargue *et al.* [8] show no indication of the presence of metallic iron. The reason for the discrepancy is not known at present, but may be related to minor differences in the annealing treatment as discussed above.

Annealing at 1100 °C results in the continued evolution of the microstructure. Fig. 11 illustrates the extent of the precipitation. The surface precipitates range from 300–600 nm long and 40–50 nm wide, Fig. 11a. The nature of the precipitation which takes place below the surface is also different. Two distinct types of subsurface precipitate are observed in a band centred around the location of the peak in the as-implanted iron distribution. Equiaxed precipitates, 4–10 nm diameter, exist together with larger precipitates which appear in weak fringe contrast in Fig. 11b. The latter class of precipitates exists over a larger range of sizes. Many of these larger precipitates are approximately equiaxed (40 nm by 40 nm). However, others appear to have grown parallel to the surface with aspect ratios as high as 6 to 1 (120 nm by 20 nm). Selected-area diffraction results from a backthinned specimen show that the large surface precipitates are Fe_2O_3 which are oriented epitactically with the Al_2O_3 substrate. Measurements of the Moiré fringes and diffraction analyses both indicate that the larger of the two types of subsurface precipitates are $(Fe, Al)_3O_4$ precipitates, again probably with the defect spinel structure. It has not been possible to identify the smaller subsurface precipitates on the basis of diffraction analysis.

Transmission electron microscopy was also used to investigate the microstructure of a specimen implanted with 4×10^{16} Fe cm^{-2} and annealed for 1 h at 1500 °C in oxygen [8]. The iron-rich subsurface precipitates produced at 1500 °C are much larger (15–50 nm in diameter) and fewer in number than those formed at $\leqslant 1100$ °C. In addition, two populations of faceted cavities were observed, one lying near the surface and one associated with the precipitates, Fig. 12. No evidence of surface precipitates was found on cross-sectioned or backthinned specimens. The results of RBS and CEMS [8] confirm the TEM observations and also indicate that more than 50% of the implanted iron has been lost from the specimen. Convergent beam electron diffraction was used to identify precipitates in a backthinned specimen. Analysis of the patterns gives values of the interplanar spacings most consistent with diamond cubic Fe_3O_4 with the [0 1 1] axis of the precipitate nearly parallel to the [0 0 0 1] axis of the Al_2O_3. However, examination of the Fe–Al–O phase diagram indicates that, given the temperature and oxygen partial pressure used, the mixed $(Fe, Al)_3O_4$ spinel or γ-Fe_2O_3 (a cubic defect spinel) are also possible. The CEMS results [8]

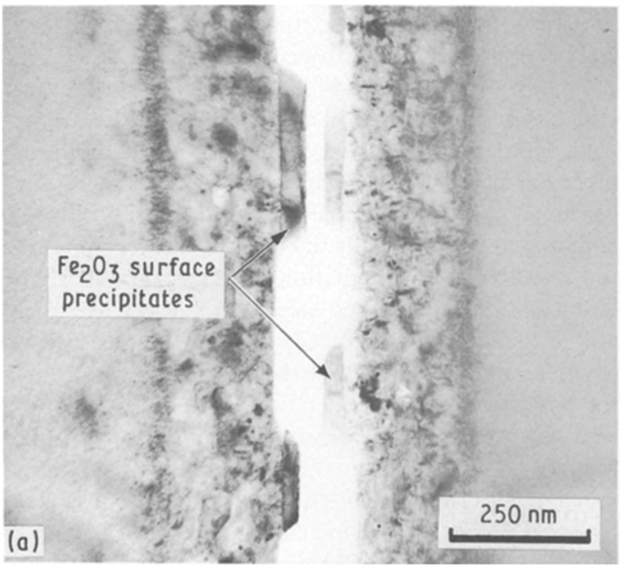

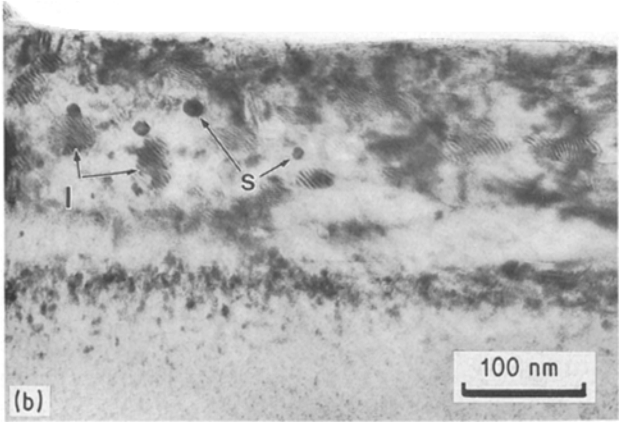

Figure 11 (a) Microstructure of α-Al_2O_3 implanted with 1×10^{17} Fe cm^{-2} and annealed for 1 h at 1100 °C in oxygen, cross-section of two specimens glued face-to-face; (b) higher magnification of specimen shown in (a), illustrating small equiaxed precipitates marked "s" and larger precipitates marked "l".

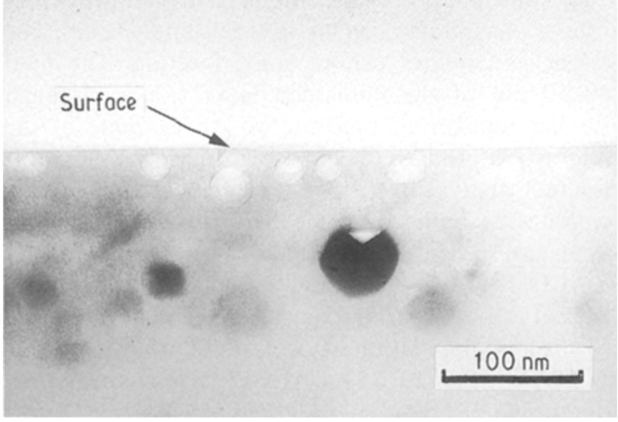

Figure 12 Microstructure of α-Al_2O_3 implanted at room temperature with 160 keV ^{56}Fe ions to a dose of 4×10^{16} Fe cm^{-2} and annealed for 1 h at 1500 °C in oxygen, cross-sectioned specimen.

indicate that all of the iron is present in the Fe^{3+} state, once again suggesting that the structure of the precipitates must be a defect spinel structure similar to the γ-Al_2O_3 type.

The extensive microstructural development which has been observed in the specimens annealed in oxygen provides some indication of the approach to equilibrium from the as-implanted state. The appearance of iron oxide phases in subsurface regions of the specimen, even at relatively low temperatures indicates that implantation-produced defects must provide mechanisms for enhanced diffusion. In addition, the observation of subsurface spinel together with surface Fe_2O_3 precipitates after anneals at 900 or 1100 °C suggests that the diffusion of oxygen into the specimen is accompanied by the counterflow of iron toward the surface. It seems reasonable that the iron originally present as metallic clusters remains relatively immobile in subsurface regions of the specimen and is oxidized in place. The analysis of CEMS results indicate that approximately 50% of the iron in as-implanted, high fluence specimens is present in these metallic clusters [8]. The remaining iron is apparently free to diffuse to the surface where it reacts with oxygen. After annealing at 1500 °C, only 50% of the implanted iron is present in large, subsurface precipitates of Fe_3O_4. The mechanism responsible for the loss of the remaining iron is not known at present. However, thermodynamic considerations suggest that melting followed by volatilization of surface oxides may occur at 1500 °C.

3.3. Annealing in 96%Ar/4% H_2

Annealing as-implanted specimens in a reducing atmosphere resulted in behaviour significantly different from that observed in an oxidizing environment. The RBS results reported by McHargue *et al.* [8] indicate recovery of the damage in the substrate. Although there is no evidence of the accumulation of iron at the surface of the specimen, the shape of the iron profile indicates some migration of the iron in the substrate at intermediate temperatures and loss of iron from the samples during the 1500 °C anneal.

Examination by TEM of a specimen implanted to 1×10^{17} Fe cm^{-2} and annealed at 900 °C in the reducing atmosphere revealed the presence of a distribution of precipitates ranging in size from 2–35 nm. The larger precipitates exhibit some faceting. The final 60–80 nm of the implanted layer exhibit a much smaller number of precipitates. An example of the microstructure is shown in Fig. 13. Selected-area diffraction analysis has been used to identify the precipitates as body-centred cubic α-Fe. These precipitates are oriented so that $\langle 110 \rangle$ α-Fe//[0001] α-Al_2O_3. However, both diffraction analysis and analysis of the Moiré fringe spacing suggest the existence of a second population of precipitates oriented so that $\langle 111 \rangle$ α-Fe // [0001] α-Al_2O_3, in agreement with the results of Ohkubo *et al.* [28]. Analysis of CEMS results indicates that the iron is distributed between small particles ($\approx$ 4 nm) and particles large enough to possess magnetic ordering ($>$ 10 nm) [34]. Continued evolution of the microstructure was observed as a result of annealing at 1100 °C. Results of CEMS [34] indicate that most of the iron is present as precipitates of α-Fe with diameters > 10 nm.

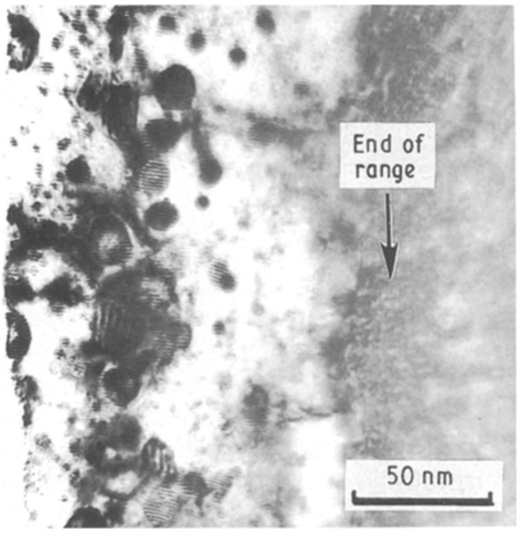

Figure 13 Microstructure of α-Al_2O_3 implanted with 1×10^{17} Fe cm^{-2} and annealed for 1 h at 900 °C in 96% Ar/4% H_2, cross-sectioned specimen.

The microstructure observed in a specimen implanted to 4×10^{16} Fe cm^{-2} and annealed in a reducing atmosphere for 1 h at 1500 °C appears to be somewhat similar to that seen in the specimen annealed at 1500 °C in oxygen. As shown in Fig. 14, the specimen contains bimodal distributions of both precipitates and cavities. In the case of the precipitates, the smaller sized population averages about 5 nm diameter and the larger sized population averages about 40 nm. There is a clear tendency for the larger cavities and precipitates to be faceted. In addition, there is a one-to-one association between the cavities and the precipitates. Convergent beam electron diffraction analyses were used to identify the precipitates as α-Fe, with the same orientation relationship as was reported above for specimens annealed at 900 °C.

In contrast to the TEM observations in specimens annealed in oxygen, TEM of specimens annealed in a reducing atmosphere showed no tendency for iron redistribution toward the surface. In fact the only microstructural change observed by TEM was the precipitation and growth of α-Fe. The one-to-one correspondence between the iron precipitates and cavities suggests that the redistribution of iron is correlated with the accumulation of vacancies into cavities. In addition, the lack of iron migration to the specimen surface during annealing in a reducing environment lends support to some of the observations made on specimens annealed in oxygen, namely the migration and precipitation of iron at the surface of a specimen is related to the counterdiffusion of oxygen into the interior of the specimen.

4. Conclusion

Analytical electron microscopy techniques have been used to investigate the microstructure of single-crystal

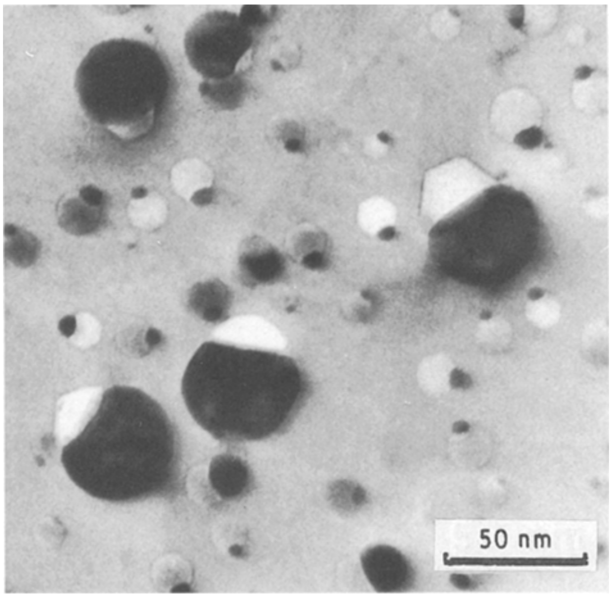

Figure 14 Microstructure of α-Al_2O_3 implanted with 4×10^{16} Fe cm^{-2} and annealed for 1 h at 1500 °C in 96% Ar/4% H_2, backthinned specimen.

α-Al_2O_3 specimens implanted at room temperature with iron ions. Particular emphasis has been placed on the microstructural development which takes place during post-implantation annealing as a function of annealing temperature and environment.

Implantation produces a heavily damaged, but crystalline, microstructure for the fluences examined. In addition, clusters of metallic α-Fe, 1–2 nm diameter, were identified in the specimen implanted to the highest dose, 1×10^{17} Fe cm^{-2}. Both the microstructure and the implanted-iron distribution undergo significant modification during subsequent anneals in oxygen. TEM examination of the microstructural evolution reveals that the changes in the iron distribution are due to diffusion (mostly towards the surface) and the formation of precipitates both on the surface and in the subsurface regions. Surface precipitates have been identified as α-Fe_2O_3, whereas subsurface precipitates have been identified as α-Fe or as various forms of spinel. This phase development is consistent with the predictions of phase diagrams and also agrees with results of previous RBS and CEMS measurements. The results suggest that the iron originally present as metallic clusters in as-implanted material remains relatively immobile in subsurface regions of the specimen and is oxidized in place. The implanted iron which has other charge states is free to diffuse to the surface where it may oxidize. At temperatures $\approx$ 1500 °C no surface precipitates are observed, indicating that they are unstable and are lost from the specimen.

Specimens annealed in a reducing atmosphere show little tendency for redistribution of iron towards the surface. The major microstructural change observed by TEM is the precipitation and growth of α-Fe.

Acknowledgements

This research was sponsored by the Division of Materials Sciences, US Department of Energy, under contract DE-AC05-84OR21400 with Martin Marietta Energy Systems, Inc. The authors thank Dr S. J. Pennycook for his assistance in obtaining the *Z*-contrast images, C. P. Haltom, A. M. Williams and A. T. Fisher for assistance in specimen preparation, and K. L. More and Drs J. Vitek and J. Bentley for useful comments on the manuscript.

References

1. G. K. HUBLER, O. W. HOLLAND, C. R. CLAYTON and C. W. WHITE (eds), "Ion Implantation and Ion Beam Processing of Materials" (North Holland, Amsterdam, 1984).
2. C. W. WHITE, C. J. McHARGUE, P. S. SKLAD, L. A. BOATNER and G. C. FARLOW, in "Materials Science Reports", Vol. 4, edited by S. S. Lau and F. W. Saris (North Holland, Amsterdam, 1989) pp. 41–146.
3. C. J. McHARGUE, C. W. WHITE, P. S. SKLAD, M. E. O'HERN, D. L. JOSLIN and G. C. FARLOW, in "Proceedings 2nd International Seminar on Surface Engineering with High Energy Beams" (Cemul, Lisbon, Portugal, 1989) pp. 561–75.
4. G. C. FARLOW, P. S. SKLAD, C. W. WHITE and C. J. McHARGUE, *J. Mater. Res.* **5** (1990) 1502.
5. G. P. PELLS and D. C. PHILLIPS, *J. Nucl. Mater.* **80** (1979) 207.
6. P. S. SKLAD, in "Ion Implantation and Plasma Assisted Processes", edited by R. F. Hochman, H. Solnick-Legg and K. O. Legg (ASM International, Metals Park, OH, 1988) pp. 149–56.
7. J. BENTLEY, *Nucl. Instrum. Meth.* **B16** (1986) 111.
8. C. J. McHARGUE, G. C. FARLOW, P. S. SKLAD, C. W. WHITE, A. PEREZ, N. KORNILIOS and G. MAREST, *ibid.* **B19/20** (1989) 813.
9. P. S. SKLAD, in "Proceedings of the Annual Electron Microscopy of America Meeting", Vol. 45, edited by G. W. Bailey (San Francisco Press, San Francisco, CA, 1989) pp. 146–7.
10. P. S. SKLAD, J. D. McCALLUM, S. J. PENNYCOOK, C. J. McHARGUE, C. W. WHITE and A. PEREZ, in "Characterization of the Structure and Chemistry of Defects in Materials", Materials Research Society Symposium Proceedings, Vol. 138, edited by B. C. Larson, M. Ruhle and D. N. Seidman (The Materials Research Society, Pittsburg, PA, 1989) pp. 119–24.
11. P. S. SKLAD, L. ROMANA, C. J. McHARGUE, C. W. WHITE and J. D. McCALLUM, *Nucl. Instrum. Meth.* **B59** (1991) 1187.
12. P. S. SKLAD, P. ANGELINI and J. SEVELY, *Phil. Mag. A*, **65** (1992) in press.
13. P. S. SKLAD, in "Proceedings of the Annual Electron Microscopy Society of America Meeting", Vol. 43, edited by G. W. Bailey (San Francisco Press, San Francisco, CA, 1989) pp. 276–9.
14. A. T. FISHER and P. ANGELINI, *ibid.* (1985) pp. 182–3.
15. J. BENTLEY, N. J. ZALUZEC, E. A. KENIK and R. W. CARPENTER, in SEM/1979/II, edited by O. Johari and R. P. Becker 1979 (SEM, AMF O'Hare, IL, 1979) pp. 581–94.
16. F. W. CLINARD, G. F. HURLEY and L. W. HOBBS, *J. Nucl. Mater.* **108**, **109** (1982) 655.
17. T. E. MITCHELL, M. R. PASCUCCI and R. A. YOUNGMAN, in "Proceedings of the Annual Electron Microscopy Society of America Meeting", Vol. 40, edited by G. W. Bailey (San Francisco Press, San Francisco, CA, 1982) pp. 600–3.
18. W. E. LEE, M. L. JENKINS and G. P. PELLS, *Phil. Mag. A* **51** (1982) 639.
19. S. J. ZINKLE, in "Processing and Characterization of Materials Using Ion Beams", Materials Research Society Symposium Proceedings, Vol. 128, edited by Lynnn E. Rehn, J. Greene and F. A. Smidt (The Materials Research Society, Pittsburg, PA, 1989) pp. 363–8.
20. S. J. ZINKLE, in "Structure-Property Relationships in Surface-Modified Ceramics", edited by C. J. McHargue, R. Kossowsky and W. O. Hofer (Kluer Academic, Dordrecht, 1989) pp. 219–29.

21. M. D. RECHTIN, *Rad. Effects* **42** (1979) 129.
22. L. W. HOBBS, *J. Amer. Ceram. Soc.* **62** (5–6) (1979) 267.
23. D. G. HOWITT and T. E. MITCHELL, *Phil. Mag. A* **44** (1981) 229.
24. W. E. LEE, K. P. D. LAGERLOF, T. E. MITCHELL and A. H. HEUER, *ibid.* **51** (1985) L23.
25. A. Y. STATHOPOULOS and G. P. PELLS, *ibid.* **47** (1983) 381.
26. N. J. ZALUZEC, in "Introduction to Analytical Electron Microscopy", edited by J. J. Hren, J. I. Goldstein and D. C. Joy (Plenum Press, New York, 1979) pp. 121–67.
27. S. J. PENNYCOOK, *Ultramicroscopy* **30** (1989) 58.
28. M. OHKUBO, T. HIOKI, N, SUZUKI, T. ISHIGURO and J. KAWAMOTO, *Nucl. Instrum. Meth.* **B39** (1989) 675.
29. C. B. CARTER and H. SCHMALZRIED, *Phil. Mag. A* **52** (1985) 207.
30. Y. K. SIMPSON and C. B. CARTER, *ibid.* **53** (1986) L1.
31. M. OHKUBO, T. HIOKI and J. KAWAMOTO, *J. Appl. Phys.* **60** (1986) 1325.
32. L. A. TIETZ and C. B. CARTER, in "Proceedings of the Annual Electron Microscopy of America Meeting", edited by G. W. Bailey (San Francisco Press, San Francisco, CA, 1987) pp. 270–1.
33. K. M. OSTYN, C. B. CARTER, M. KOEHNE, H. FALDE and H. SCHMALZRIED, *J. Amer. Ceram. Soc.* **67** (1984) 679.
34. C. J. McHARGUE, P. S. SKLAD, C. W. WHITE, G. C. FARLOW, A. PEREZ and G. MAREST, *J. Mater. Res.*, **6** (1991) 2145.

Received 3 September
and accepted 28 November 1991